



Ag supported on electrospun macro-structure CeO₂ fibrous mats for diesel soot oxidation

Chanmin Lee^a, Joo-Il Park^b, Yong-Gun Shul^c, Hisahiro Einaga^{a,*}, Yasutake Teraoka^a

^a Department of Molecular and Material Sciences, Interdisciplinary Graduate School of Engineering Sciences, Kyushu University, Kasuga, Fukuoka 816-8580, Japan

^b Petroleum Research Center, Kuwait Institute for Scientific Research (KISR), P.O. Box 24885, Safat 13109, Kuwait

^c Department of Chemical and Biomolecular Engineering, Yonsei University, 50 Yonsei-ro, Seodaemun-gu, Seoul 120-749, Republic of Korea

ARTICLE INFO

Article history:

Received 12 November 2014

Received in revised form 2 March 2015

Accepted 5 March 2015

Available online 7 March 2015

This work is dedicated to the memory of Professor Yasutake Teraoka, who passed away unexpectedly on July 2th, 2014.

Keywords:

Ceria

Silver

Fibrous catalyst

Diesel soot oxidation

Electrospinning

ABSTRACT

Ceria oxide (CeO₂) nanofibers with diameters of 241–253 nm were produced via the electrospinning method. They were then applied as new support materials for silver nanoparticles and their effectiveness as diesel soot oxidation catalysts was examined. The crystal structure of the Ag was confirmed by X-ray diffraction (XRD), X-ray photoelectron spectroscopy (XPS), high-resolution transmission electron microscopy (HR-TEM), and energy dispersive spectroscopy (EDS). The diesel soot oxidation experiment was performed using a mixture of carbon black and the fabricated catalyst. In the tight contact and loose contact modes, the highest temperatures of both the CeO₂-fiber-supported Ag catalysts (Ag/CeO₂) calcined at 500 °C and the CeO₂ fibers calcined at 500 °C were shifted to a lower temperature range, compared with JRC-CEO-3 (a commercial catalyst). In addition, the activation energy also showed similar behavior. Thus, the fibrous CeO₂ and Ag/CeO₂ have been shown to be effective and promising catalysts for soot oxidation.

© 2015 Elsevier B.V. All rights reserved.

1. Introduction

The diesel internal combustion engine is one of the most environmentally-friendly vehicle devices, because it emits less carbon dioxide (diesel, 13.4 kg/km; gasoline, 16.6 kg/km) and is more fuel efficient (diesel, 183.1 MJ/100 km; gasoline, 223.5 MJ/100 km) than the universal gasoline stoichiometric engine [1]. However, considerable challenges still exist regarding the emission control of particulate matter (PM), commonly known as soot, expelled by the diesel combustion process. These ultrafine particles, which have aerodynamic diameters of less than 2.5 μm (PM 2.5), are problematic as they can cause serious respiratory diseases, including lung cancer and chronic obstructive pulmonary disease (COPD) [2,3].

Currently, diesel particulate filter (DPF) systems are commonly used as PM controllers, because of their non-catalytic trapping structure that can physically capture the soot in the exhaust [4,5]. However, as with other filters, they require a regeneration system to eliminate the accumulated PM, in order to consistently

maintain the filter performance [6]. Although a number of regeneration methods to resolve this problem have been reported [7], they are not perfectly satisfactory. For example, a regeneration method using nitrogen dioxide is not effective, because sufficient nitrogen dioxide is not supplied under normal combustion operating conditions [8]. In addition, methods involving the direct oxidation of PM have been studied. However, a high temperature (above 500 °C) is required for this regeneration and DPFs can be destroyed by extreme thermal conditions [9]. As a result of these ongoing issues, catalytic soot oxidation for DPFs has been explored in various alternative methods to overcome these limitations. A range of catalysts for effective soot oxidation have been studied, particularly platinum group metal (PGM)-free catalysts, which include pure oxides [10,11], perovskites [12,13] and spinel oxide [14] catalysts, alkali [15,16] and alkali earth-metal catalysts [17], as well as cerium oxide catalysts [18]. Of these, cerium-based catalysts have been widely suggested for effective accelerated soot oxidation, since cerium oxides with fluorite structure can be created for use in the redox transfer of Ce³⁺ and Ce⁴⁺ ion states. This involves the ability to release and store atomic oxygen [19]. For this reason, cerium [18,20], cerium-composites (e.g., CeO₂/ZrO₂ [21,22]), and cerium-supported metal catalysts (e.g., K/CeO₂ [23,24], Ag/CeO₂

* Corresponding author. Tel.: +81 92 583 7525; fax: +81 92 583 8853.
E-mail address: einaga.hisahiro.399@m.kyushu-u.ac.jp (H. Einaga).

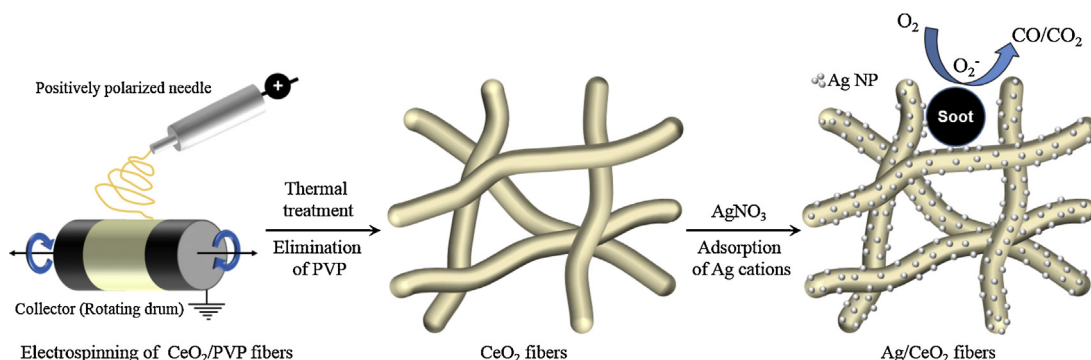


Fig. 1. Schematic illustration of Ag/CeO₂ nanofiber synthesis sequence. CeO₂ nanofibers were fabricated through the electrospinning of spinnable Ce/PVP in a DMF/EtOH precursor solution, followed by thermal treatment. Ag was then loaded on the surfaces of the CeO₂ nanofibers.

[25,26], Co/CeO₂ [27,28], and Cu/CeO₂ [29]) have been investigated as potential diesel soot oxidation catalysts.

In order to create a cerium-supported metal catalyst, a synthesis procedure is required. As a synthetic method, electrospinning is a very convenient and versatile method that uses an electric charge to fabricate nanofiber mats with one-dimensional nanostructure [30,31]. Since the development of electrospinning, this technique has been principally applied to the synthesis of polymeric fibers [32]. Following further research, TiO₂ nanofiber was first introduced by Lia and Xia [33] and, since then, various inorganic and/or inorganic-organic nanofibers have been reported in the past decade [34,35]. These ceramic nanofibers are generally prepared by electrospinning and thermal treatment [36], and exhibit dominant characteristics such as three-dimensional matrix morphology, hierarchical porous structure, and high surface area [37]. In addition, electrospun nanofibers are used in various applications, for example, as catalysts [38] and filtration membranes [39] and in high performance sensors [40,41] and energy conversion systems (e.g., as proton exchange membranes for fuel cells [42], electrodes for dye-sensitized solar cells [43], or lithium ion batteries [44]). In general, electrospun nanofiber mats exhibit high porosity [45], depending on the structure of the inter-fiber space, with diameters ranging in size from a few hundred nanometers to several micrometers range. Hence, the change of morphology from particles to fibers can significantly increase the catalytic reaction surface area [46–48], especially in the case of macropore-sized feed reactions, such as soot oxidation. For catalysts, increased pore size means that an ingress of soot into the inner pores can occur and also leads to a significant increase in the catalyst/soot contact area.

In this study, we prepared CeO₂ nanofibrous mats with uniform three-dimensional structure and large pore size (>50 nm, macroporous structure) via the electrospinning technique. Then, silver nanoparticles were loaded on the surface of the prepared CeO₂ nanofiber to accelerate the catalytic oxidation of the diesel soot. To improve the diesel soot oxidation performance, catalysts with different calcination temperatures were evaluated and compared with a commercial CeO₂ catalyst (JRC-CEO-3, Japan Reference Catalyst).

2. Experimental

2.1. Chemicals and preparation of catalysts

Cerium (III) nitrate hexahydrate (Ce(NO₃)₃·6H₂O, 99%), polyvinylpyrrolidone (PVP, MW = 1,300,000), N, N-dimethylformamide (DMF, 99.9%), ethanol (99.9%), and carbon black were purchased from Sigma–Aldrich. Silver nitrate (AgNO₃, 99.8%) was obtained from Kishida Chemical.

Fig. 1 illustrates the overall synthesis process of the Ag/CeO₂ nanofibers. Firstly, CeO₂ nanofibers were prepared via a typical electrospinning process followed by a heat treatment. Then, 1.5 g of Ce(NO₃)₃·6H₂O and 0.83 g of PVP were mixed in a 5.6 g DMF and 1.4 g ethanol solution (weight ratio of DMF and EtOH: 8:2) which was vigorously stirred at room temperature for 3 h. PVP was used as a guiding polymer and viscosity controller for the formation of a uniform fibrous structure, because it has remarkable characteristics such as high molecular weight and high solubility in polar solvents. Next, the precursor solution was carefully electrospun onto a regular rotating drum collector with a spinneret tip-to-drum distance (between the needle tip and drum collector) of 15 cm. The spinnable solution was injected into the thin needle tip (30 G, 0.15-mm inner diameter) at a constant supply of 15 μL min^{−1}, and an 18-kV voltage was applied. This led to the formation of a uniform fibrous structure under specific optimized conditions without droplets and/or beads. During the electrospinning process, the temperature and humidity were maintained at approximately 30 °C and below 30% RH, respectively. The collected nanofibers were calcined at 500, 800, or 1000 °C for 6 h with a heating rate of 1 °C min^{−1} in an air atmosphere to perfectly eliminate the polymer substance (PVP) and obtain pure CeO₂ nanofibers. After heat treatment, silver (4.5 wt%) was loaded on the surface of the CeO₂ fibers, as follows: (1) 0.6 g of CeO₂ fibers were added to 0.0445 g of AgNO₃ in 100 ml of pure water; (2) the mixture was stirred at 250 °C for approximately 1.5 h to evaporate the pure water; (3) The obtained substance was heat-treated at 250 °C for 2 h in air to completely decompose the metal salts; (4) The fibers were calcined at 500 °C for 5 h with a heating rate of 3.34 °C min^{−1} [25]. Hereafter, the pure CeO₂ fibers calcined at 500, 800, and 1000 °C are labeled CeO₂-500, CeO₂-800, and CeO₂-1000, respectively. Similarly, Ag/CeO₂-500, Ag/CeO₂-800, and Ag/CeO₂-1000 are used to refer to the silver-loaded CeO₂ nanofibers calcined at 500, 800, and 1000 °C, respectively.

2.2. Catalyst characterization

The morphologies of the electrospun CeO₂ and Ag/CeO₂ nanofibers were analyzed by means of a scanning electron microscope (SEM; JSM-6710F, JEOL), while the crystal structures of the catalysts were analyzed using X-ray diffraction (XRD; RINT 2000, RIGAKU). The intensity peaks were recorded at a 2θ range from 25 to 100 ° with a scan speed of 10 min^{−1}. In order to measure the BET surface area, nitrogen sorption was performed at −196 °C using a BELSORP II (BEL). Prior to the nitrogen sorption measurement, the samples were degassed under vacuum conditions at 200 °C for 3 h. Mercury intrusion porosimetry measurements were performed using an Autopore III 9400 (Micromeritics). High-resolution transmission electron microscopy (HRTEM) analysis and energy dispersive spectroscopy (EDS) mapping were

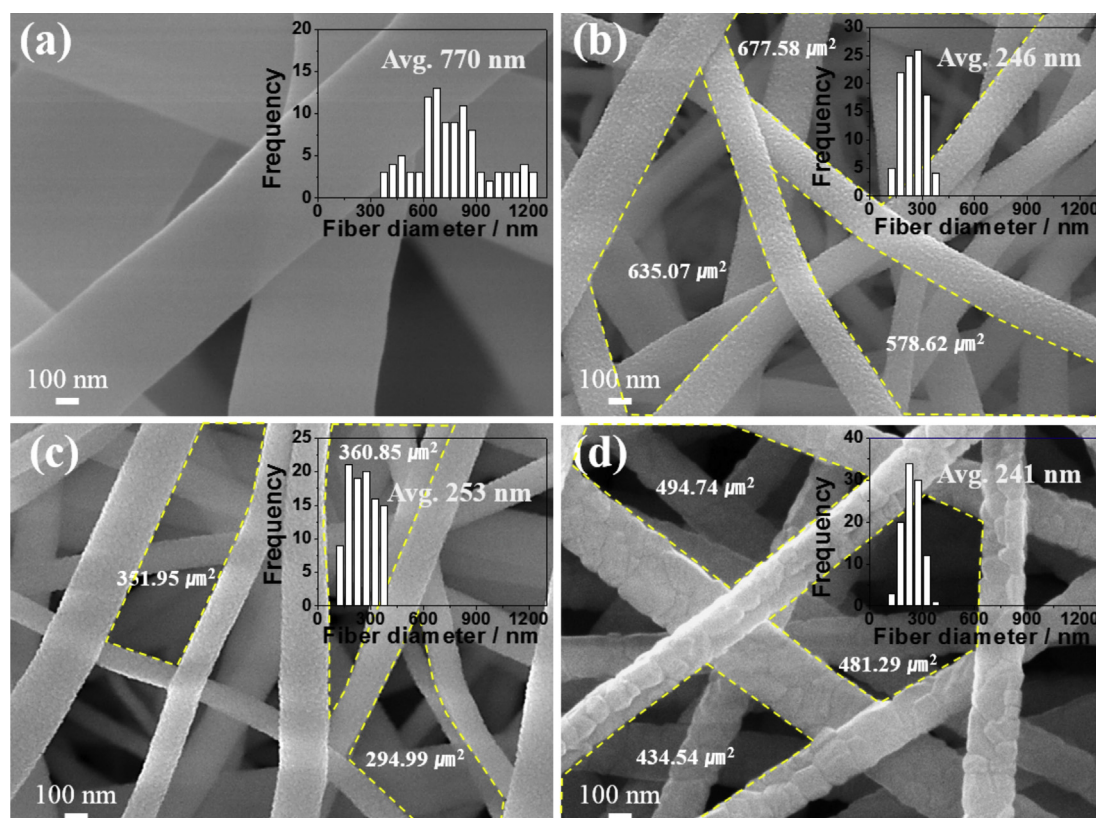


Fig. 2. SEM images of electrospun nanofibers (inset: fiber diameter distribution): (a) CeO₂/PVP nanofibers, (b) CeO₂-500, (c) CeO₂-800, and (d) CeO₂-1000.

performed using a JEM-2100F (JEOL) at an accelerating voltage of 200 kV. The samples (dispersed in ethanol) were stored in an ultrasonic bath for 20 min and then dropped on a carbon-coated copper grid. Then, X-ray photoelectron spectroscopy (XPS) was conducted via a K-alpha (Thermo VG Scientific, UK) under vacuum conditions (7.8×10^{-9} mbar). A monochromated Al X-ray source (Al $\text{K}\alpha$ line at 1486.6 eV) at an X-ray power of 36 W was used, and all binding energies were calibrated based on the C 1s peak at 284.8 eV for sample charge compensation. The obtained spectra were fitted using the Fityk-software with the Gaussian function.

2.3. Preparation of diesel soot simulated model and combustion performance test

A simulated model diesel soot substance was prepared by mixing 5 wt% carbon black with the prepared catalyst and then applied to two types of contact mode (tight contact (TC) and loose contact (LC)) [49]. For the TC mode sample, the catalyst and carbon black were intensively mixed using an agate mortar for 10 min, while, in the LC mode case, the catalyst and carbon black were thoroughly mixed by spatula for 10 min. To evaluate the soot oxidation performance, a thermogravimetric analysis (TGA) of the soot oxidation reaction was performed using a Shimadzu DTG-60 with a temperature range of 120–800 °C and a heating rate of 10 °C min⁻¹ in an air atmosphere (21% O₂ and 79% N₂, 100 mL min⁻¹). The characteristic temperatures were analyzed from the TG/DTG curve using the following measurements: (i) weight loss starting point (T_{ig}), (ii) highest point (T_{max}), and (iii) finishing point (T_{f}). Note that, when two T_{max} peaks were observed, inter alia, the higher peak was defined as $T_{\text{max,H}}$ and the lower peak was designated as $T_{\text{max,L}}$.

2.4. Soot oxidation activation energy

The activation energy (ΔE) was measured via the Ozawa method from the TGA data [50]. The catalyst and soot mixture (95:5 weight ratio) was measured over a temperature range of 120–800 °C with heating rates (Φ) of 5, 10, 20, and 30 °C min⁻¹ in an air atmosphere. The value of the absolute temperature (T_{α}), at which a fixed fraction, α , of the soot is combusted for each heating rate, was obtained from the TG curve. The activation energy can be calculated from the fitted least square of the $\log \Phi$ versus T_{α}^{-1} data series, using the following equation

$$\log \Phi = B - 0.4567 \left(\frac{E_a}{RT_{\alpha}} \right), \quad (1)$$

where B is a constant value with regards to the reaction.

3. Results and discussion

3.1. Synthesis and characterization of Ag/CeO₂ nanofibrous catalyst

The morphology of the fibrous structure (Fig. 2) was characterized using SEM, showing images and fiber diameter distribution of both the CeO₂/PVP (before calcination) and the CeO₂ nanofibers (after calcination). The average diameters of the CeO₂ fiber after calcination exhibited a narrow distribution, together with a reduced diameter, in comparison with that of the CeO₂/PVP. Each of the 100 selected samples showed a reduction in average diameter from 770 nm (28.1% relative standard deviation (RSD), CeO₂/PVP) to 246 nm (24.9% RSD, CeO₂-500), 253 nm (29.6% RSD, CeO₂-800), and 241 nm (21.7% RSD, CeO₂-1000). This reduction in average diameter suggests that the distance between the inter-particulates in the fiber decreased due to the removal of the PVP.

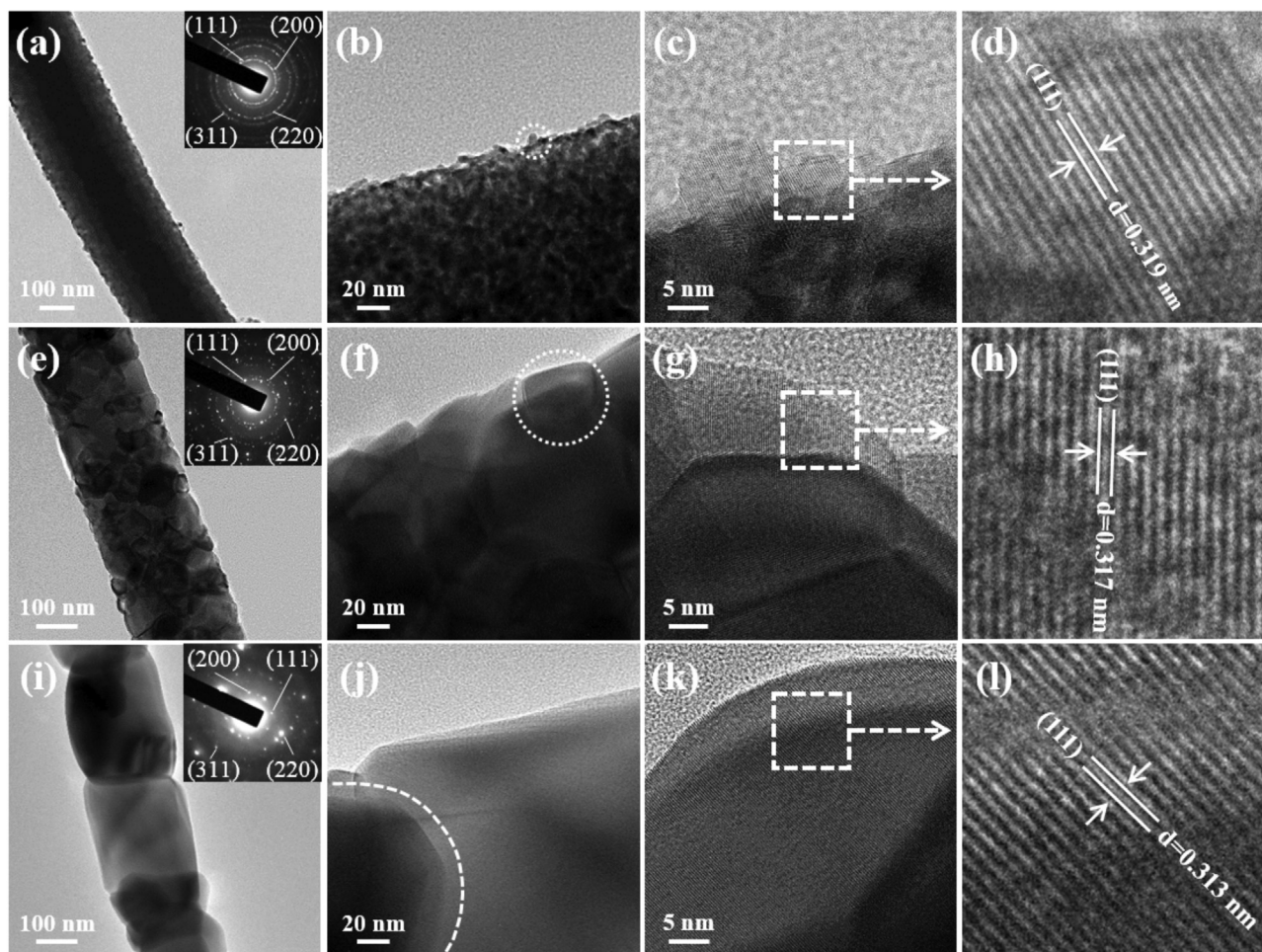


Fig. 3. HR-TEM images of CeO₂ nanofibers (inset: SAED patterns): (a–d) CeO₂-500, (e–h) CeO₂-800, and (i–l) CeO₂-1000.

Effect of calcination temperature (500, 800, and 1000 °C) on the crystallizability and micro-structure of the CeO₂ nanofibers was investigated using high resolution transmission electron microscopy (HRTEM), as shown in Fig. 3. For the CeO₂-500 samples, a grain size of less than 10 nm inside the CeO₂ fibers was observed (Fig. 3b), while the CeO₂-800 and CeO₂-1000 fibers displayed a large crystalline morphology structure (Fig. 3f and j, respectively), exhibiting a growth in CeO₂ grain size in response to calcination temperature. It can be speculated that the surface area of the CeO₂-500 fiber was significantly higher than that of the other samples, as shown in Table 1 (see Fig. 3a, e, and i). The inset images of Fig. 3a, e, and i show the selected area electron diffraction (SAED) patterns, which indicate that the CeO₂ fibers exhibit mainly polycrystalline ring diffraction patterns, corresponding to the (1 1 1), (2 0 0), (2 2 0), and (3 1 1) facets. Note that this is in full agreement with the XRD results (Fig. 5a). Furthermore, lattice fringes of 0.319 (500 °C), 0.317 (800 °C) and 0.313 (1000 °C) nm, representing the (1 1 1) plane in a CeO₂ face-centered cubic (fcc) structure, can be observed in Fig. 3d, h, and l, respectively [51,52].

To investigate the inter-pore size of the fibers, mercury porosimetry was conducted on the CeO₂ in particle form (JRC-CEO-3) and the CeO₂ fibrous structures, as indicated in Fig. 4. In the case of JRC-CEO-3, two characteristic pore-size peaks were observed at approximately 10 nm (mesopore, between 2 and 50 nm) and 0.9 μm (macropore). In contrast, the pore sizes of CeO₂-500, CeO₂-800, and CeO₂-1000 were distributed at approximately from 0.2 nm to 90 μm, indicating the formation of macropores with large size (above 1 μm). In particular, pore size of CeO₂-500 were shifted

to above 3 μm in contrast with the CeO₂-800 and CeO₂-1000. It might be more likely due to the calcination temperature. Besides, the diameter of carbon black was average 37.9 nm (shown in Supplementary Fig. S1). This implies that the macropores are more favorable than micropores in soot oxidation. For these results, this suggests that CeO₂ fiber is a more desirable structure for use in the soot oxidation reaction, in comparison with the particle form. This can be attributed to the increased contact area between the catalyst and soot, leading to easy diffusion and transferability of molecules in inner pores [53].

Table 1

Surface area and catalytic performance data for prepared samples under TC (tight contact) and LC (loose contact) modes.

Catalyst	S _{BET} ^a (m ² g ⁻¹)	Soot oxidation performance (°C) ^b							
		TC mode				LC mode			
		T _{ig}	T _{max}	T _f		T _{ig}	T _{max,L}	T _{max,H}	T _f
CeO ₂ -500	20.4	294	429	497		376	465	596	631
CeO ₂ -800	3.45	379	504	571		424	530	633	662
CeO ₂ -1000	3.40	381	513	578		433	536	639	664
Ag/CeO ₂ -500	5.07	292	429	495		387	–	481	569
Ag/CeO ₂ -800	3.07	371	484	556		395	–	485	568
Ag/CeO ₂ -1000	2.74	382	496	563		405	–	514	596
JRC-CEO-3	81.94	332	448	530		487	–	606	689

^a Specific surface area.

^b Definition of T_{ig} (starting temperature of soot ignition), T_{max} (maximum temperature), T_{max,L} (lower maximum temperature), T_{max,H} (higher maximum temperature), and T_f (finished temperature of soot oxidation).

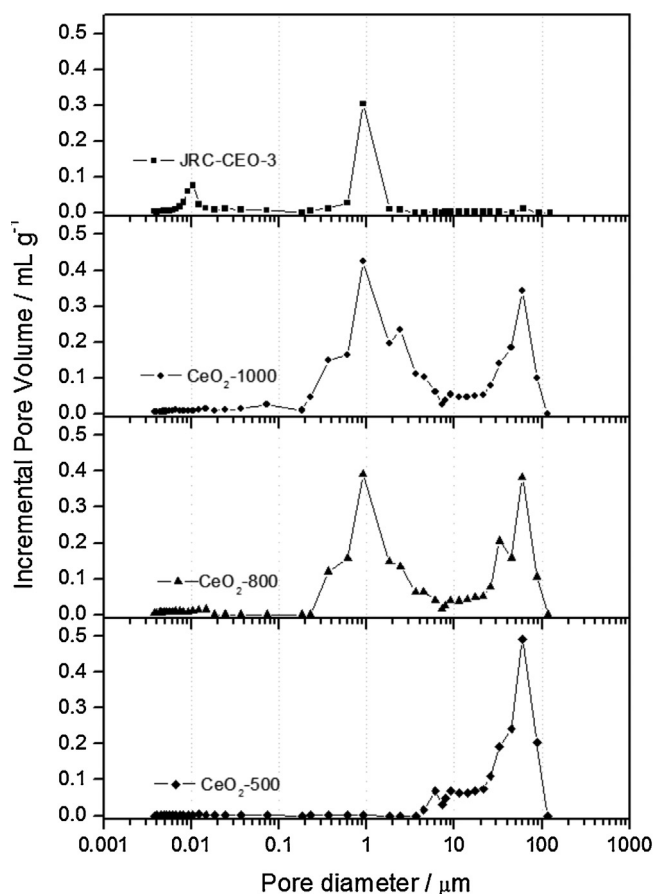


Fig. 4. Pore size distribution of CeO₂-500, CeO₂-800, CeO₂-1000, and JRC-CEO-3 from mercury porosimetry.

Fig. 5 shows the XRD patterns of CeO₂ and Ag/CeO₂ fibers according to calcination temperature. Although the CeO₂-500 fibers show small diffraction peaks, the XRD patterns clearly illustrate a general crystalline pattern, indicating the cubic fluorite structure of CeO₂ (JCPDS card No. 43-1002), as shown in Fig. 5a. In addition, as the calcination temperatures were increased, the crystallinity of the CeO₂ phase was improved. For the Ag/CeO₂ fibers, diffraction peaks corresponding to (1 1 1), (2 0 0), and (2 2 0) facets of crystalline Ag (JCPDS card No. 04-0783) became clearly apparent with increasing calcination temperature (see Fig. 5b). This result indicates that the Ag particles were successfully supported on the CeO₂ fibers without a change in crystalline structure and, of the Ag crystal faces analyzed, Ag (111) in particular was occupied.

Energy dispersive spectroscopy (EDS) mapping and HRTEM images (Fig. 6) were analyzed to determine the micro-structure of the Ag/CeO₂-500 and the surface composition of the fibers. As can be seen in Fig. 6 Fig. 6b and c, Ag/CeO₂-500 is irregularly composed of two elemental components of Ag (red spots) and Ce (white spots) atoms. Further evidence of Ag deposition on the CeO₂ fiber was provided by the overall EDS spectrum results, which clearly shows the silver and cerium peaks (Fig. 6a). The HRTEM images of the Ag/CeO₂-500 were taken under high magnification and are shown in Fig. 6d, e, and f. The observed lattice fringe at 0.242 nm corresponded to the (1 1 1) Ag crystal plane, while another fringe at 0.314 nm coincided with the Ce (1 1 1) plane [54]. In other words, it reveals that the Ag nanoparticles of about 10 nm were homogeneously loaded on the CeO₂ fiber.

Finally, Fig. 7a shows the binding energy deconvolution for the Ag 3d peaks of the Ag/CeO₂-500 samples. Two peaks due to the presence of Ag were observed for the Ag/CeO₂ fiber, while no peak

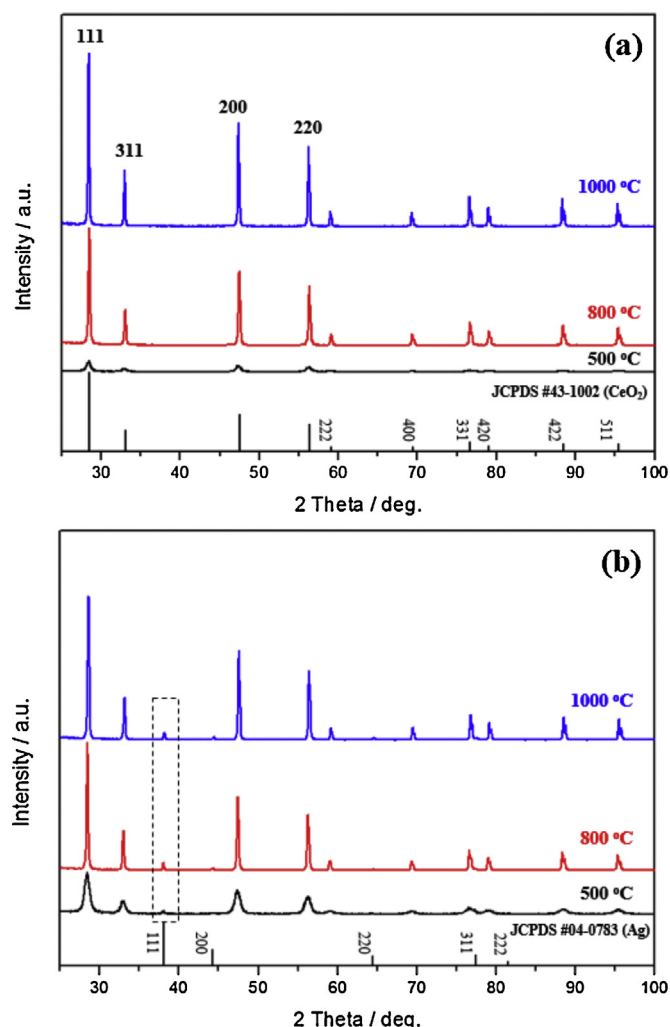


Fig. 5. XRD patterns: (a) CeO₂ and (b) Ag/CeO₂ nanofibers.

of the CeO₂ fiber appeared in the Ag 3d region (Fig. 7a). Among them, the new peaks at 368.1 and 374.1 eV can be attributed to Ag 3d_{5/2} and Ag 3d_{3/2}, respectively, and are associated with metallic Ag [55]. Obviously, the gap of 6.0 eV between the two peaks also indicates a metallic form [56]. It has been reported that gas phase oxygen over metallic Ag can be transformed to active oxygen species, which are involved in carbon oxidation [57–60].

As shown in Fig. 7b, the O 1s spectrum of the CeO₂ fiber was fitted into two peaks: one at a low binding energy of 529.3 eV, which is related to lattice oxygen (O²⁻), and the other peak at a binding energy of 531 eV, which is associated with surface adsorbed oxygen (O⁻) [61,62]. However, in contrast with the CeO₂ fiber, the XPS spectra of O 1s in the Ag/CeO₂ fiber were shifted slightly to the binding energies of 529.2 and 530.8 eV. In addition, we estimated the ratio of O_{surface}/O_{lattice} for CeO₂ and Ag/CeO₂ to study whether catalytic activity is favorable. The obtained values were 0.94 and 1.25 for the CeO₂ and Ag/CeO₂ fiber, respectively. It is considered that the Ag loading can probably enhance a catalytic activity due to the increased surface oxygen [26].

3.2. Soot oxidation performance evaluated via TGA

Fig. 8 and Fig. S2 show the TG and DTG curves for diesel soot oxidation for the CeO₂, Ag/CeO₂ fibrous catalyst, and JRC-CEO-3 without Ag (reference catalyst) samples in the LC (loose contact) and TC (tight contact) modes. The measured values of T_{ig} , T_{max} ,

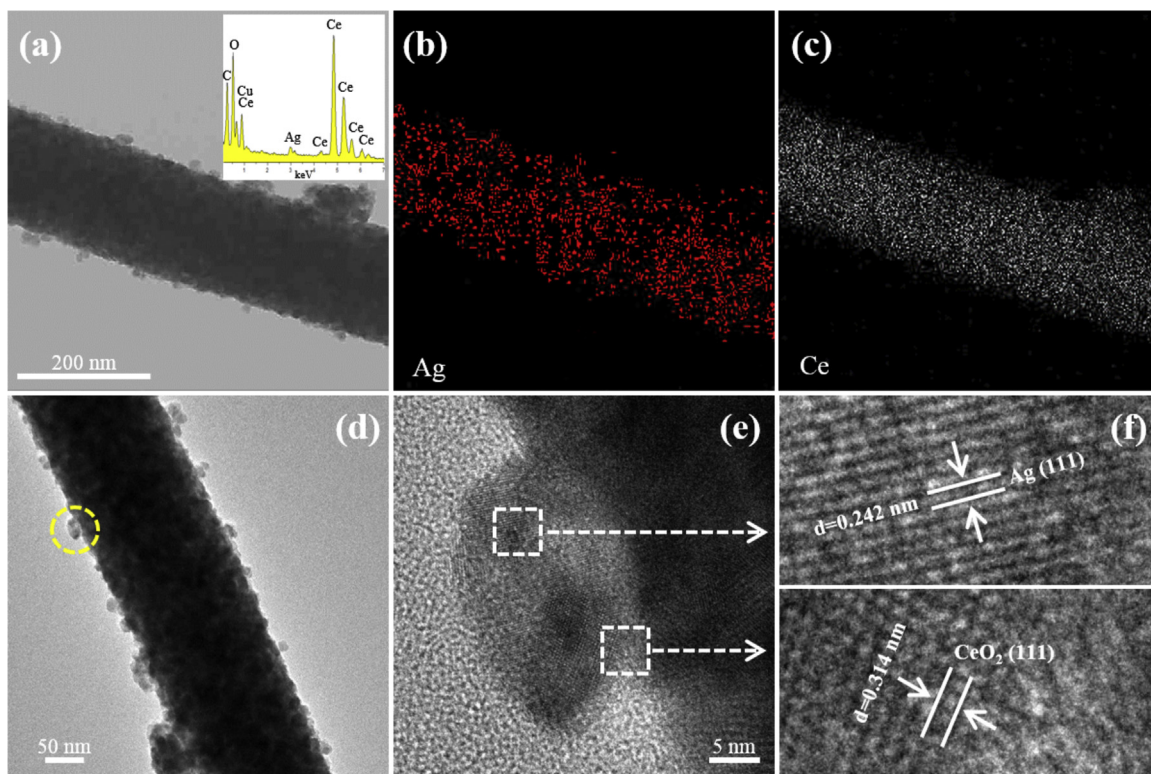


Fig. 6. DES and HR-TEM images of Ag/CeO₂-500 nanofibers: (a–c) DES (inset: EDS spectrum) and (d–f) HR-TEM images.

and T_f from the TGA are listed in Table 1. Under the TC mode, it can be seen that the measured maximum temperatures of CeO₂ for soot oxidation (T_{max}) increased from 429 to 513 °C with an increase in calcination temperature to 500, 800, and 1000 °C. Additionally, the T_{ig} values (soot ignition starting temperature) of CeO₂-500, CeO₂-800, and CeO₂-1000 were recorded at 294, 379, and 381 °C, respectively, while the soot oxidation completion temperatures (T_f) were observed at 497, 571, and 578 °C, respectively. Similarly, the observed values of T_{ig} , $T_{max,L}$, $T_{max,H}$, and T_f in the LC mode showed greater conformity with increasing calcination temperature. Under the LC mode, two maximum temperatures ($T_{max,L}$ and $T_{max,H}$) were observed. It can be speculated that the lower temperature ($T_{max,L}$) is associated with the oxidation reaction due to contact between the soot and catalyst (catalytic combustion), while the higher temperature ($T_{max,H}$) is related to the oxidative response of the carbon (non-catalytic combustion) [25]. These results indicate that increasing the calcination temperature gave rise to the

decrease in surface area of CeO₂ due to the sintering. Hence, the increasing surface areas of the CeO₂ catalysts play important roles in the catalytic oxidation. Additionally, Fig. S3 shows the relationship between T_{max} and specific surface area (BET) of JRC-CEO3 calcined at 500, 800 and 1000 °C, respectively. The surface area decreased from 82 to 12 m² g⁻¹, while T_{max} increased from 606 to 637 °C under the LC mode. This finding suggested that the large surface area which can increase the contact area between the soot and catalyst also correlate with the catalytic activity.

The TG and DTG curves of the Ag/CeO₂ fibers are shown in Fig. 8d, e, and f. Here, the T_{max} values of Ag/CeO₂-500, Ag/CeO₂-800, and Ag/CeO₂-1000 were found to be 429, 481, and 496 °C in the TC mode, respectively, while T_{max} in the LC mode was observed at 487, 485, and 614 °C, respectively. Although the T_{max} value of Ag/CeO₂-500 was equal to that of CeO₂-500 in the TC mode, due to compact mixing of the catalyst and carbon black in the TC mode, the overall performance of the Ag/CeO₂ fibers was generally higher than that of

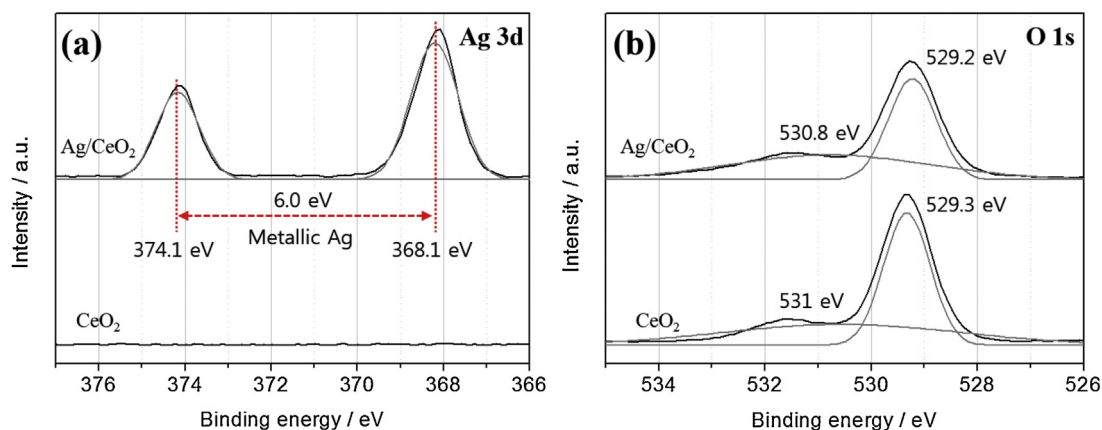


Fig. 7. XPS spectra of CeO₂-500 and Ag/CeO₂-500 nanofiber surfaces: (a) Ag 3d and (b) O 1s.

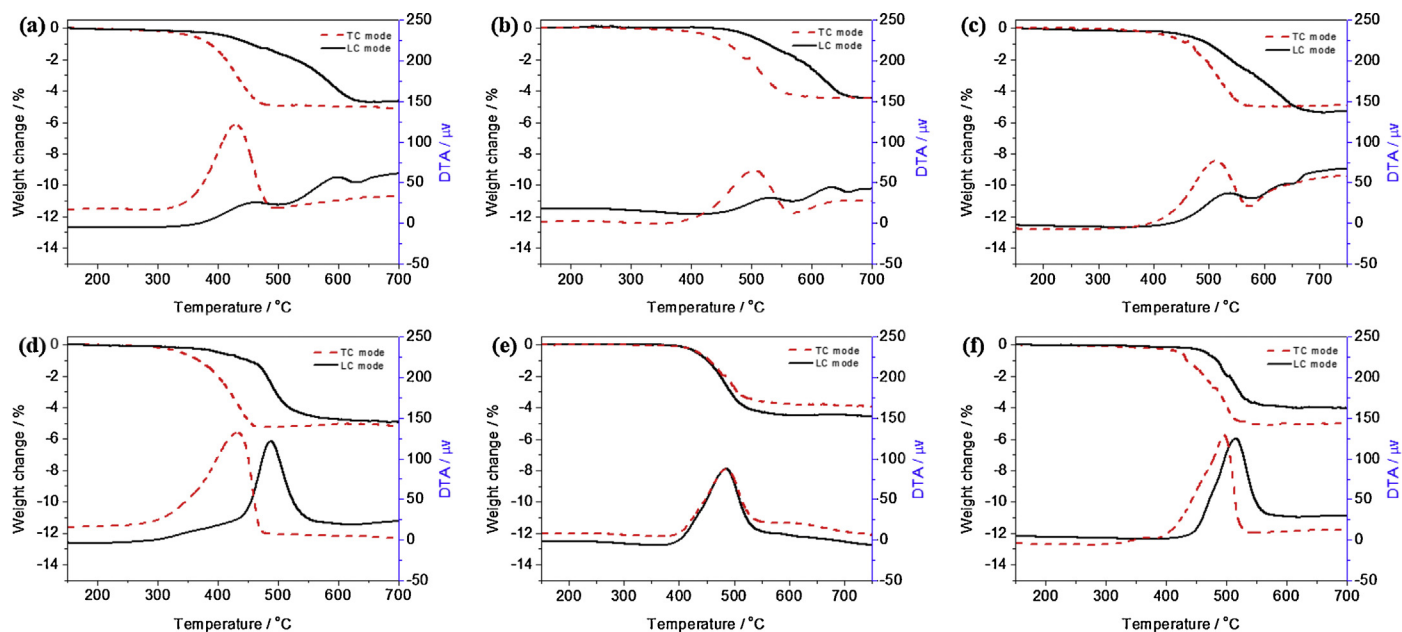


Fig. 8. TG and DTG curves: (a) CeO₂-500, (b) CeO₂-800, (c) CeO₂-1000, (d) Ag/CeO₂-500, (e) Ag/CeO₂-800, and (f) Ag/CeO₂-1000.

the CeO₂ fibers (support only) under both LC and TC modes. These results clearly demonstrate that the enhancement of catalytic property depended not only the increase in catalyst surface area but also the Ag deposition [25]. In general, the combustion temperature of the LC mode was higher than that of the TC mode, suggesting that the active oxygen transport of the TC mode was more efficient than that of the LC mode.

As can be seen in Table 1 and Fig. S2, the T_{\max} of JRC-CEO-3 was much higher than that of CeO₂-500 and Ag/CeO₂-500 in both the TC (17–19 °C) and LC modes (10–140 °C), it was indicated that the change of morphology and Ag deposition enhanced catalytic soot oxidation performance [63–66].

3.3. Activation energy

In order to study the reaction kinetics, analysis of the activation energy (ΔE) was conducted using Ozawa plots from the TGA curves. Fig. S4 shows the ΔE and Ozawa plots of $\log \Phi$ versus T^{-1} for soot oxidation conversion of 20 to 80%. As shown in Fig. 9, the activation energies of Ag/CeO₂-500, CeO₂-500, and JRC-CEO-3 were

evaluated at 50% soot conversion under the TC mode. The activation energies of Ag/CeO₂-500 and CeO₂-500 were found to be 112.1 (average ΔE of 113.7 kJ mol⁻¹, from 20 to 80%) and 123.2 kJ mol⁻¹ (average ΔE of 124.5 kJ mol⁻¹), respectively. On the other hand, the ΔE value of JRC-CEO-3 was 130.1 kJ mol⁻¹ (average ΔE of 135.7 kJ mol⁻¹). These results indicate that the activation energy of Ag/CeO₂-500 was generally lower than that of CeO₂-500 and of JRC-CEO-3. Although the surface area of Ag/CeO₂ was considerably lower than that of CeO₂ or of JRC-CEO-3, the catalysis efficiency was significantly enhanced. This can be explained by the consideration that both the surface area and the specific metallic species of Ag used in the catalysts are important factors for enhancing soot oxidation performance [25,26].

4. Conclusion

In summary, we proposed and demonstrated a fibrous catalyst composed of large macroporous CeO₂ with Ag particles for diesel soot oxidation, which were successfully prepared via the electrospinning method. The Ag/CeO₂ and CeO₂ fibrous catalysts calcined at 500 °C exhibited improved catalytic performance for soot oxidation, in comparison with the commercially available catalyst (JRC-CEO-3). This was due to their large pore size, which is related to the macroporous characteristics of the porous mat structure in CeO₂. In addition, our present study revealed that the large surface areas of CeO₂ and metallic species of Ag can contribute to high soot oxidation activity. Therefore, the proposed fibrous CeO₂ and Ag/CeO₂ demonstrated and evaluated in this study can be recommended as promising catalysts for soot oxidation.

Acknowledgement

This work was supported by JSPS KAKENHI Research Project Number 26630413.

Appendix A. Supplementary data

Supplementary data associated with this article can be found, in the online version, at <http://dx.doi.org/10.1016/j.apcatb.2015.03.008>.

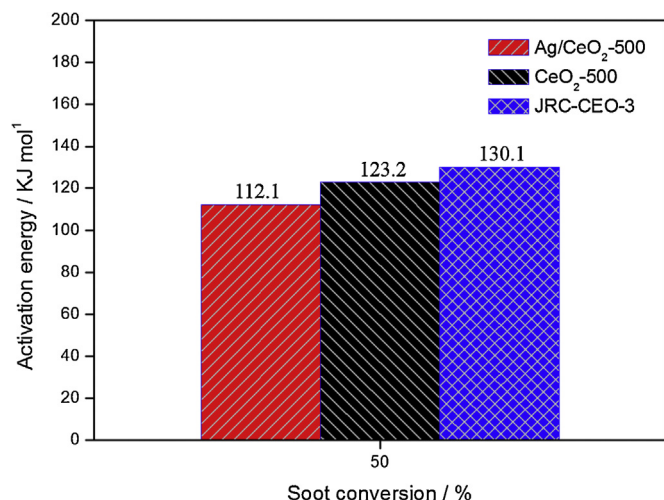


Fig. 9. Activation energy of 50% soot oxidation under tight contact (TC) mode.

References

- [1] Annual Certification Test Results and Data. United States Environmental Protection Agency, Washington (DC); 2005.
- [2] G. Viegi, S. Maio, F. Pistelli, S. Baldacci, L. Carrozzi, *Respirology* 11 (2006) 523.
- [3] H. Li, X. Qian, Q. Wang, *Environ. Sci. Technol.* 47 (2013) 13210.
- [4] A.P. Walker, *Top. Catal.* 28 (2004) 165.
- [5] B.A.A.L. van Setten, M. Makkee, J.A. Moulijn, *Catal. Rev.* 43 (2001) 489.
- [6] G.C. Koltsakis, A.M. Stamatelos, *Prog. Energy Combust. Sci.* 23 (1997) 1.
- [7] C. Görsmann, *Monatsh. Chem./Chem. Mon.* 136 (2005) 91.
- [8] H. Dwyer, A. Ayala, S. Zhang, J. Collins, T. Huai, J. Herner, W. Chau, *J. Aerosol Sci.* 41 (2010) 541.
- [9] J.C. Caroca, F. Millo, D. Vezza, T. Vlachos, A. De Filippo, S. Bensaid, N. Russo, D. Fino, *Ind. Eng. Chem. Res.* 50 (2010) 2650.
- [10] I. Atribak, A. Bueno-López, A. García-García, P. Navarro, D. Frías, M. Montes, *Appl. Catal. B Environ.* 93 (2010) 267.
- [11] I. Atribak, I. Such-Basáñez, A. Bueno-López, A. García, *J. Catal.* 250 (2007) 75.
- [12] Y. Teraoka, K. Nakano, W. Shangquan, S. Kagawa, *Catal. Today* 27 (1996) 107.
- [13] H. Shimokawa, H. Kusaba, H. Einaga, Y. Teraoka, *Catal. Today* 139 (2008) 8.
- [14] L. Xue, C. Zhang, H. He, Y. Teraoka, *Appl. Catal. B Environ.* 75 (2007) 167.
- [15] Y. Zhang, X. Zou, *Catal. Commun.* 8 (2007) 760.
- [16] H. An, P.J. McGinn, *Appl. Catal. B Environ.* 62 (2006) 46.
- [17] L. Castoldi, R. Matarrese, L. Lietti, P. Forzatti, *Appl. Catal. B Environ.* 90 (2009) 278.
- [18] K. Krishna, A. Bueno-López, M. Makkee, J.A. Moulijn, *Appl. Catal. B Environ.* 75 (2007) 189.
- [19] J. Stubenrauch, J.M. Vohs, *J. Catal.* 159 (1996) 50.
- [20] A. Bueno-López, K. Krishna, M. Makkee, J.A. Moulijn, *Catal. Lett.* 99 (2005) 203.
- [21] L. Zhu, J. Yu, X. Wang, *J. Hazard. Mater.* 140 (2007) 205.
- [22] L. Katta, P. Sudarsanam, G. Thrumurthulu, B.M. Reddy, *Appl. Catal. B Environ.* 101 (2010) 101.
- [23] C.A. Neyertz, E.E. Miró, C.A. Querini, *Chem. Eng. J.* 181–182 (2012) 93.
- [24] M.L. Pisarello, V. Milt, M.A. Peralta, C.A. Querini, E.E. Miró, *Catal. Today* 75 (2002) 465.
- [25] H. Shimokawa, Y. Kurihara, H. Kusaba, H. Einaga, Y. Teraoka, *Catal. Today* 185 (2012) 99.
- [26] K. -i. Shimizu, H. Kawachi, A. Satsuma, *Appl. Catal. B Environ.* 96 (2010) 169.
- [27] J. -d. Liu, T. Jin, W. Li, X.-F. Sun, H.-R. Guan, Z.-Q. Hu, *J. Alloys Comp.* 457 (2008) 185.
- [28] M. Dhakad, T. Mitshuhashi, S. Rayalu, P. Doggali, S. Bakardjiva, J. Subrt, D. Fino, H. Haneda, N. Labhsetwar, *Catal. Today* 132 (2008) 188.
- [29] D. Courcot, E. Abi-Aad, S. Capelle, A. Aboukaïs, *Stud. Surf. Sci. Catal.* 116 (1998) 625.
- [30] A. Frenot, I.S. Chronakis, *Curr. Opin. Colloid Interface Sci.* 8 (2003) 64.
- [31] A. Greiner, J.H. Wendorff, *Angew. Chem. Int. Ed.* 46 (2007) 5670.
- [32] D.H. Reneker, I. Chun, *Nanotechnology* 7 (1996) 216.
- [33] D. Li, Y. Xia, *Nano Lett.* 3 (2003) 555.
- [34] B. Ding, H. Kim, C. Kim, M. Khil, S. Park, *Nanotechnology* 14 (2003) 532.
- [35] I.S. Chronakis, *J. Mater. Process. Technol.* 167 (2005) 283.
- [36] Y. Dai, W. Liu, E. Formo, Y. Sun, Y. Xia, *Polym. Adv. Technol.* 22 (2011) 326.
- [37] D. Li, Y. Xia, *Adv. Mater.* 16 (2004) 1151.
- [38] E. Formo, E. Lee, D. Campbell, Y. Xia, *Nano Lett.* 8 (2008) 668.
- [39] X.-H. Qin, S.-Y. Wang, *J. Appl. Polym. Sci.* 102 (2006) 1285.
- [40] I.-D. Kim, A. Rothschild, *Polym. Adv. Technol.* 22 (2011) 318.
- [41] I.-D. Kim, A. Rothschild, B.H. Lee, D.Y. Kim, S.M. Jo, H.L. Tuller, *Nano Lett.* 6 (2006) 2009.
- [42] C. Lee, S.M. Jo, J. Choi, K.-Y. Baek, Y.B. Truong, I.L. Kyratzis, Y.-G. Shul, *J. Mater. Sci.* 48 (2013) 3665.
- [43] M.Y. Song, D.K. Kim, K.J. Ihn, S.M. Jo, D.Y. Kim, *Nanotechnology* 15 (2004) 1861.
- [44] C. Kim, K.S. Yang, M. Kojima, K. Yoshida, Y.J. Kim, Y.A. Kim, M. Endo, *Adv. Funct. Mater.* 16 (2006) 2393.
- [45] W.-J. Li, C.T. Laurencin, E.J. Caterson, R.S. Tuan, F.K. Ko, *J. Biomed. Mater. Res.* 60 (2002) 613.
- [46] E. Formo, P.H.C. Camargo, B. Lim, M. Jiang, Y. Xia, *Chem. Phys. Lett.* 476 (2009) 56.
- [47] S. Zhan, D. Chen, X. Jiao, Y. Song, *Chem. Commun.* (2007) 2043.
- [48] A.C. Patel, S. Li, C. Wang, W. Zhang, Y. Wei, *Chem. Mater.* 19 (2007) 1231.
- [49] J.P.A. Neeft, M. Makkee, J.A. Moulijn, *Appl. Catal. B Environ.* 8 (1996) 57.
- [50] T. Ozawa, *Bull. Chem. Soc. Jpn.* 38 (1965) 1881.
- [51] M. Han, X. Wang, Y. Shen, C. Tang, G. Li, R.L. Smith, *J. Phys. Chem. C* 114 (2010) 793.
- [52] N. Barrabeis, K. Föttinger, J. Llorca, A. Dafinov, F. Medina, J. Saí, C. Hardacre, G. Rupprechter, *J. Phys. Chem. C* 114 (2010) 17675.
- [53] S. Li, R. Kato, Q. Wang, T. Yamanaka, T. Takeguchi, W. Ueda, *Appl. Catal. B Environ.* 93 (2010) 383.
- [54] Z. Wang, S. Zhao, S. Zhu, Y. Sun, M. Fang, *CrystEngComm* 13 (2011) 2262.
- [55] C.S. Fadley, D.A. Shirley, *J. Res. Natl. Bur. Stand. Sect. A: Phys. Chem. A* 74 (1970) 543.
- [56] C. Gunawan, W.Y. Teoh, C.P. Marquis, J. Lifia, R. Amal, *Small* 5 (2009) 341.
- [57] A. Nagy, G. Mestl, *Appl. Catal. A Gen.* 188 (1999) 337.
- [58] N. Güngör, S. Işci, E. Günister, W. Mišta, H. Teterycz, R. Klimkiewicz, *Appl. Clay Sci.* 32 (2006) 291.
- [59] Z. Qu, M. Cheng, X. Dong, X. Bao, *Catal. Today* 93–95 (2004) 247.
- [60] M. Machida, Y. Murata, K. Kishikawa, D. Zhang, K. Ikeue, *Chem. Mater.* 20 (2008) 4489.
- [61] A.M. Salvi, F. Decker, F. Varsano, G. Speranza, *Surf. Interface Anal.* 31 (2001) 255.
- [62] P. Ji, J. Zhang, F. Chen, M. Anpo, *J. Phys. Chem. C* 112 (2008) 17809.
- [63] P.A. Kumar, M.D. Tanwar, S. Bensaid, N. Russo, D. Fino, *Chem. Eng. J.* 207–208 (2012) 258.
- [64] S. Bensaid, N. Russo, D. Fino, *Catal. Today* 216 (2013) 57.
- [65] P. Miceli, S. Bensaid, N. Russo, D. Fino, *Nanoscale Res. Lett.* 9 (2014) 1.
- [66] P.A. Kumar, M.D. Tanwar, N. Russo, R. Pirone, D. Fino, *Catal. Today* 184 (2012) 279.